Confluentes Mathematici, Vol. 3, No. 3 (2011) 523–541

DOI: 10.1142/S1793744211000382

World Scientific
www.worldscientific.com

HYDRO-ELASTIC WAVES IN A COCHLEAR MODEL: NUMERICAL SIMULATIONS AND AN ANALYTICALLY REDUCED MODEL

WILLIAM R. HOLMES*, MICHAEL JOLLY†
and JACOB RUBINSTEIN‡

Department of Mathematics,
Indiana University, 831 E. 3rd
Bloomington, IN 47401, USA
**wrholmes@math.ubc.ca*
†*msjolly@indiana.edu*
‡*jrubist@indiana.edu*

Received 17 November 2010

A three-dimensional model of the hydro-elastic waves in the mammalian cochlea is presented along with numerical simulations. The cochlear fluid is treated as linear, incompressible, and inviscid. The cochlear partition is treated as a massless thin plate loaded by the fluid. This model is then reformulated by analytically removing the fluid variable with the use of a Dirichlet-to-Neumann operator. The resulting fifth-order nonlocal PDE for the motion of the partition is simulated using a novel implicit numerical scheme. Simulations demonstrate that this model exhibits traveling wave characteristics and a clear place principle. Asymptotic analysis in the small aspect ratio of the cochlea is performed on the given model equations with energetic concerns in mind. The results of simulations along with these asymptotic arguments suggest a relationship between the form and function of the cochlea which we compare to physiological data.

Keywords: Ear model; numerical simulation; thin plate; Dirichlet-to-Neumann operator; cochlea; reduced model.

AMS Subject Classification: 35Lxx, 65Mxx, 92Cxx

1. Introduction

The inner ear is one of the most fascinating organs in our body. It converts mechanical vibrations arriving from the ear drum into neural signals that are transmitted into the auditory cortex. The main body in the inner ear is the cochlea, a complex fluid-filled, coiled organ. The transduction of mechanical information in the cochlea occurs as follows. Sound pressure waves cause excitation of the eardrum. The eardrum is mechanically connected to the cochlea at the oval window through

*Corresponding author, also at Department of Mathematics, University of British Columbia.
‡Also at Department of Mathematics, Technion, Haifa, Israel.

a set of three small bones (ossicles). Vibrations of the eardrum are thus transferred directly to the cochlea. The vibration of the oval window causes pressure fluctuations in the cochlear fluid. These pressure waves in turn excite vibrations of a plate (basilar membrane) which partitions the fluid-filled cavity. These vibrations take a particular form which is referred to as the "place principle". That is, a pure tone input frequency yields a vibration profile highly localized in space at a "characteristic place" along the partition. This characteristic place is located at the apical end for low input frequencies and monotonically moves toward the basel end as the frequency is increased. This place principle induces frequency dependent transduction of neural signals in hair cells which lie atop the partition. For an exposition on the mechanics of hearing, see [5, 15].

Numerous models have been proposed for the hydro-elastic waves propagating in the cochlea. While a complete list is outside the scope of this paper, we do point out some features of these models which are pertinent to this discussion. The most widely used and published class of models are those of the transmission line type [14, 13, 12]. These models assume the cochlear partition is a one-dimensional object consisting of a collection of point oscillators coupled only through the fluid. They attempt to capture the passive response of the basilar membrane to waves in the fluid. However, it is widely believed that a passive response is too weak to create the observed neural stimulus. Furthermore, nonlinear effects such as tonal suppression and frequency doubling have been observed in the cochlear response. Therefore it has been suggested that part of the basilar membrane response is due to an active internal mechanism that enhances the passive response. To account for this, a class of active models such as [19, 7] layer nonlinearities on top of these passive transmission line models.

In order to more accurately capture the mechanics of the partition, others such as [10, 17] have made attempts to treat it as an elastic plate coupled to a three-dimensional fluid. Such models subsequently assume a simplistic functional form for the plate displacement, effectively removing the associated biharmonic operator from the problem. The most complete treatment of elasticity in the cochlea problem can be seen in [4]. This treatment considers the cochlear partition to be a fully elastic structure with curvature. Due to the comprehensive nature of the underlying model and the explicit numerical treatment of the cochlear fluid inherent in the immersed boundary method, it requires substantial computational resources and, to our knowledge, has not been expanded upon.

Our goal in this paper is twofold. We first seek to solve numerically a complete set of equations describing the water waves in a three-dimensional cochlea, coupled to the vibrations of a two-dimensional nonhomogeneous plate. We concentrate on the simple case of a passive cochlea with an inertial fluid, and put our efforts into extending the existing treatments of the plate. We assume that the vibrations are of small amplitude and thus use a linear model. Our equations are formulated in Sec. 2. Then, in Sec. 3 the fluid equations are integrated via a Dirichlet-to-Neumann (DtN) operator. We are thus left with a nonlocal equation for the plate's

deflection function. In addition to the difficulty induced by the nonlocality, the equation is essentially fifth-order, taking into account the plate nature of the basilar membrane. An implicit numerical scheme, which appears to be novel in this setting, for solving the plates equation is described in Sec. 4. It is based on the explicit form of the DtN operator and on a very efficient and accurate scheme for the biharmonic operator. The numerical scheme is tested for convergence and accuracy in Sec. 5. In Sec. 7, we present simulations of the full model. Our solutions exhibit a clear "place principle" in the sense that as the frequency of the driving force increases, the maximal deflection of the basilar membrane shifts to the basal end of the cochlea.

A second goal of this work, presented in Sec. 6, is to produce a more informative asymptotic reduction of the three-dimensional model equations. Substantial efforts in the literature have been dedicated to the production of such models due to difficulties associated with fully three-dimensional models. Much of the variation in these models occurs in the treatment of the fluid with little additional consideration of the mechanics of the plate. We integrate the dynamic elasticity of the cochlear plate into our model reduction. The resulting asymptotic model effectively treats the fluid in similar fashion to that of transmission line type models, but retains information regarding the elastic nature of the plate. In Sec. 7, we use simulations of the full cochlear model to validate these asymptotics. In Sec. 8, we discuss a novel physiological result relating the cochlear aspect ratio to the size of the perceptible hearing range in mammals. This result is initially seen in the presented asymptotic reduction, verified in simulations of the three-dimensional model equations, and compared to experimental data.

2. The Model

The cochlea is a long, thin, coiled tube consisting of three fluid-filled cavities and a complex micro-structure, which is forced at one end by the input from the eardrum. We make a few simplifying assumptions on the geometry. We first assume that the cochlea can be unwound without dramatically affecting its function. It is known that the spiral shape does affect cochlear function at low frequencies [11], however this is more a tuning effect than a dramatic functional effect. We further assume that the fluid effects of the two larger cavities (scala vestibula, scala tympani) dominate those of the third smaller cavity which we neglect. As the two remaining cavities are roughly equal in area, we take them to be identical rectangular boxes. We assume these two boxes are separated by a single rectangular partition known as the basilar membrane which serves as a platform for the motion sensing mechanism of the cochlea (Organ of Corti). We assume that the partition fully separates the two cavities, thus neglecting the helicotrema. We neglect the Organ of Corti as it is believed to play only a minor role in the passive mechanics of the cochlea.

Thus, our physical system consists of a long, thin, fluid-filled rectangular box with a partition separating it into two cavities. In reality, the cochlea tapers off

toward the apical end. This feature, together with varying stiffness of the cochlea, is responsible for the dispersion in the place principle. To simplify the numerical treatment, we neglect the tapering of the cochlea. It is a straightforward matter to add the tapering feature into the one-dimensional reduction in Sec. 6 through a change of variables. This would effectively augment the form of the stiffness coefficient but not its decaying feature, which is responsible for the place principle.

The fluid motions are assumed to be small in relation to the dimensions of the problem, so we take the fluid model to be linear. For simplicity we further assume that it is irrotational, inviscid, and incompressible. For the cochlea, compressibility and viscosity are complicated topics. Evidence suggests compressibility does play a role in the function of the system [9] and it has been argued that while present, viscosity is not important [6]. Since our goal is to better understand the role of elasticity and the cochlear aspect ratio, we make these assumptions as a starting point. We thus take the fluid to be governed by the simplified Euler equations

$$\rho\phi_t + P = 0, \tag{2.1}$$

$$\triangle\phi = \triangle P = 0, \tag{2.2}$$

where $P(x, y, z, t)$ is the fluid pressure, $\phi(x, y, z, t)$ is the fluid velocity potential, and ρ is the fluid density which is assumed to be constant. For the moment we defer the discussion of boundary conditions for the fluid.

We take the cochlear partition to be a thin plate. This is at odds with the term basilar membrane, but it is known that the partition exhibits plate-like characteristics as opposed to membrane-like characteristics [2]. Consider the cochlear partition at rest to fill the domain $(x, y, 0) \in [0, L_x] \times [0, L_y] \times [-L_z, L_z]$ and the two cavities to fill the domains above and below the partition. Further assume that the input forcing occurs at the $x = 0$ face of the top cavity. We allow the plate to have variable friction $r(x)$ and stiffness $k(x)$ where the variation is only present in the longitudinal direction as is observed [2]. It is also assumed that the energetic effects of plate friction, stiffness, and fluid inertia dominate the inertial effects of the plate so we neglect the mass of the plate. While this simplifies the equations, it does not dramatically alter the analysis or computations. We have observed numerically that including the plate's inertia moderately sharpens the response. Thus our plate is governed by

$$r(x)w_t + \triangle(k(x)\triangle w) = -P_u(x, y, 0, t) + P_l(x, y, 0, t) = \rho\phi_{t_u} - \rho\phi_{t_l}, \tag{2.3}$$

where $w(x, y, t)$ is the vertical displacement of a point on the plate located at position (x, y) and the subscripts u and l denote the fluid properties in the upper and lower cavities respectively. Here we are assuming the plate is loaded by the pressure difference across the plate and that the bi-harmonic operator represents the tendency for the thin plate to resist deformation [8]. In assuming that the plate interacts only with the fluid pressure at $z = 0$, we are essentially assuming that the motions of the plate are small in relation to the dimensions of the problem. This

is in line with the treatment of the plate as thin and the fluid as linear. We take clamped plate boundary conditions

$$\begin{aligned} w, w_x &= 0, \quad x = 0, L_x, \\ w, w_y &= 0, \quad y = 0, L_y, \end{aligned} \tag{2.4}$$

as it is assumed to be rigidly attached to the cochlear walls.

Notice that the loading of the plate by the fluid is only dependent on the difference in pressure across the partition. We decompose P, and correspondingly ϕ as

$$P_u(x, y, z, t) = P_m(x, y, t) + P^u(x, y, z, t), \tag{2.5}$$

$$P_l(x, y, z, t) = P_m(x, y, t) + P^l(x, y, z, t), \tag{2.6}$$

where $P_m(x, y, t)$ is the mean cross-sectional pressure. Let us further assume that the fluid is antisymmetric about the plate so that $P^l(x, y, -z, t) = -P^u(x, y, z, t)$. This is a standard assumption taken along with incompressibility and can be seen in [5] for example. At this point we drop the superscripts and from now on write $P = P^u$ and $\phi = \phi^u$. Then the equation for the motion of the plate can be reduced to

$$r(x)w_t + \triangle(k(x)\triangle w) = -2P = 2\rho\phi_t. \tag{2.7}$$

Given this reduction we can remove the bottom cavity from the model so that our model now consists of a single fluid-filled cavity with an elastic plate at the bottom boundary shown in Fig. 1.

A brief note on the meaning of plate friction r is in order. This feature is at best not well understood and at worst unphysical. While it is known that the cochlear fluid provides a significant source of energy dissipation, it is unknown what effects, if any, the mechanics of the basilar membrane have on energy dissipation. Due to our treatment of the cochlear fluid as inviscid, it is however necessary to include it. This is a widely used assumption [14, 1, 12] due to the difficulty in dealing with more complicated fluid mechanical models.

Before writing down the boundary conditions for the fluid, we need to choose whether to work with a potential-based formulation or a pressure-based formulation. On the surface, these appear different, but these differences are superficial in

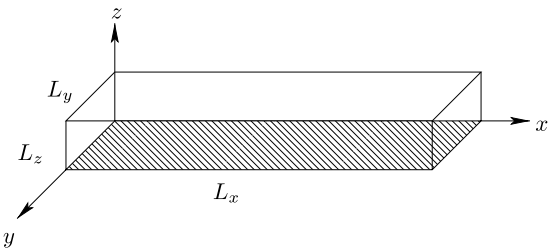

Fig. 1. The geometrically simplified single cavity cochlea. The forcing is understood to occur at the $x = 0$ boundary and the cochlear partition fills the $z = 0$ face.

nature. The fluid used in this model acts only to distribute the forcing at the oval window to the length of the plate which is the object of interest. To this end, the fluid is coupled to the plate in two ways. First, the pressure of the fluid in contact with the plate produces a load. Second, the continuity condition implies the plate's velocity must equal the fluid velocity at each point. The underlying form of these couplings is independent of the formulation of the fluid used. That said, the potential formulation does produce a model which is more symmetric in the sense that time derivatives of both w and ϕ appear. This feature will be of use when discussing an asymptotic model. We thus choose to use the velocity potential formulation.

We now take the following set of boundary conditions for ϕ

$$\phi(0,y,z,t) = F(y,z,t), \qquad \phi(L_x,y,z,t) = 0, \tag{2.8}$$

$$\phi_y(x,0,z,t) = 0, \qquad \phi_y(x,L_y,z,t) = 0, \tag{2.9}$$

$$\phi_z(x,y,0,t) = w_t(x,y,t), \quad \phi_z(x,y,L_z,t) = 0, \tag{2.10}$$

where $-\rho F_t = f$ and f is the force applied by the oval window. The boundary conditions at the $x = 0, L_x$ faces are force-matching or pressure boundary conditions while the remaining faces take velocity-matching conditions. Note that in moving from a pressure condition at the $x = 0, L_x$ faces to a potential condition, the time integration yields constants. These constants simply induce extraneous time independent solutions of the Laplace problem which do not interact with the plate. So they are not included. From a physical perspective, it would be sensible to prescribe Neumann velocity conditions on all faces. Such boundary conditions allow reference pressures to creep into the problem which interact with the plate however. At least one pressure condition is necessary to avoid this issue. The basal ($x = 0$) pressure condition is a natural choice. The apical ($x = L_x$) pressure condition is chosen as representative of the helicotrema. However, it has been observed that in past models, the specific form of the apical boundary condition has little effect on the function of the model [12]. Further, the computational model to be discussed can handle either case. Thus we take our model to be

$$\triangle\phi(x,y,z,t) = 0, \tag{2.11}$$

$$r(x)w_t(x,y,t) + \triangle(k(x)\triangle w(x,y,t)) = 2\rho\phi_t(x,y,0,t), \tag{2.12}$$

along with boundary conditions for the plate and pressure given by (2.4) and (2.8)–(2.10). We shall comment on the initial conditions later when discussing numerics.

3. Dirichlet to Neumann Formulation

At this juncture we reformulate the model in a way that will make the numerical solution simpler. Recall that we are primarily interested in observing the motion of the plate. It is seen in (2.10) and (2.12) that the plate interacts only with the potential and its normal derivative at the $z = 0$ face. So it is unnecessary to carry

the full-fluid equations throughout the problem. Instead we analytically eliminate the potential and end up with a nonlocal equation for the plate's deflection w. Before proceeding further, let us assume that the forcing to the system $F(y,z,t) = F(t)$ is time-dependent only. This piston-like treatment of the forcing is not strictly necessary. However, it simplifies the resulting model and there is little reason to think that the spatial profile of the forcing effects the function of the system, particularly so in light of the small aspect ratio of the cochlea. Under this assumption, we can restate (2.10) as

$$w_t(x,y,t) = \bar{T}\phi(x,y,0,t), \tag{3.1}$$

where $\bar{T}$ is a Dirichlet-to-Neumann (DtN) operator for the given potential Laplace problem.

In order to compute this operator $\bar{T}$, let us first homogenize the forcing boundary condition at the $x = 0$ face. Define

$$q(x,t) = F(t)\frac{x - L_x}{L_x} \tag{3.2}$$

and

$$\phi^\star(x,y,z,t) = \phi(x,y,z,t) + q(x,t). \tag{3.3}$$

Then $\phi^\star$ is harmonic and inherits all of the boundary conditions of ϕ with the exception of the forcing boundary condition at $x = 0$ which is now homogeneous Dirichlet. Consider the Laplace problem for $\phi^\star$ with fictitious boundary conditions given by

$$\phi^\star(0,y,z,t) = 0, \qquad \phi^\star(L_x,y,z,t) = 0, \tag{3.4}$$

$$\phi^\star_y(x,0,z,t) = 0, \qquad \phi^\star_y(x,L_y,z,t) = 0, \tag{3.5}$$

$$\phi^\star(x,y,0,t) = g(x,y,t), \quad \phi^\star_z(x,y,L_z,t) = 0, \tag{3.6}$$

where g is an arbitrary function. It can be found directly through the use of separation of variables that

$$\phi^\star_z(x,y,0,t) = -\sum_{m,n=0}^{\infty,\infty} \beta_{n,m}(t) s_{n,m}\pi \tanh(s_{n,m}\pi L_z) \sin\frac{n\pi x}{L_x}\cos\frac{m\pi y}{L_y}, \tag{3.7}$$

where

$$s_{n,m} = \left(\left(\frac{n}{L_x}\right)^2 + \left(\frac{m}{L_y}\right)^2\right)^{\frac{1}{2}} \tag{3.8}$$

and $\beta_{n,m}$ are the expansion coefficients of g in the basis $\{\sin\frac{n\pi x}{L_x}\cos\frac{m\pi y}{L_y}\}$. Define

$$\bar{T}g(x,y,t) := \phi^\star_z(x,y,0,t). \tag{3.9}$$

This operator $\bar{T}$ converts Dirichlet data at the $z = 0$ face into Neumann data in a manner which is compatible with the Laplace problem and boundary conditions at the remaining faces.

We can now repose the problem in the following way

$$w_t = \phi_z(x, y, 0, t) = \bar{T}\phi^\star(x, y, 0, t), \tag{3.10}$$

$$r(x)w_t + \triangle(k(x)\triangle w) = 2\rho\phi_t^\star - 2\rho q_t(x, t). \tag{3.11}$$

Applying $\bar{T}$ to Eq. (3.11) and substituting for $\phi^\star$, we can reduce this to a single wave type equation involving only w

$$2\rho w_{tt} - \bar{T}(r(x)w_t + \triangle(k(x)\triangle w) + 2\rho q_t(x, t)) = 0. \tag{3.12}$$

The wave nature of Eq. (3.12) is clear. A slightly less clear observation is that this is a fifth-order PDE. This is a result of the presence of the fourth-order biharmonic operator along with $\bar{T}$ which encodes a derivative and is linearly unbounded. As expected, in the absence of true plate inertia, the fluid inertia supplies the necessary resonance structure for wave-type characteristics to exist. The expected nonlocality due to the fluid is expressed in the operator $\bar{T}$. The fluid equations are fully encoded in the operator $\bar{T}$ and in $q_t(x, t)$. This also means that it is straightforward to replace our fluid model by another model such as Stokes equations.

It is possible at this point to make a shallow water approximation to the operator $\bar{T}$

$$\bar{T} \approx L_z\triangle_{(x,y)}. \tag{3.13}$$

While this approximation is well founded, it is not beneficial in this case. The shallow water operator is essentially quadratically unbounded while $\bar{T}$ is linearly unbounded. Further, as will be discussed, $\bar{T}$ can be computed efficiently so that it is comparable in computation time to $\triangle$.

4. Numerical Implementation

Suppose the plate fills $(x, y) \in [0 : L_x, 0 : L_y]$ and the computational domain is discretized into $(N + 1) \times (M + 1)$ points. Let $\Delta x = \frac{L_x}{N}$, $\Delta y = \frac{L_y}{M}$, and $w_{i,j}^n = w(x_i, y_j, t_n)$ where $t_n = n\Delta t$. The close relation of (3.12) to the wave equation inspires the numerical scheme to be discussed. As a first pass, an explicit scheme using a leapfrog treatment of the time derivatives was used. This scheme was successful but suffered from a stringent stability condition of $O(\Delta x^{5/2})$. This is due to the essentially fifth-order nature imposed by the biharmonic operator and the linearly unbounded $\bar{T}$ representing a fifth spatial derivative.

In order to remove this stability issue, a fully implicit scheme was developed for this system. For the purposes of this formulation, we will utilize matrix forms of the given operators. Along these lines, let us denote the DtN by the matrix operator T and the non-constant stiffness operator by L. As well, let R be the diagonal friction matrix. Then upon discretization of the spatial part of the problem, (3.12) can be reposed as

$$2\rho\mathbf{w}_{tt} - T(R\mathbf{w}_t + L\mathbf{w} + 2\rho\mathbf{q}_t(t)) = 0. \tag{4.1}$$

We use a standard Crank–Nicolson procedure for the temporal part of the problem yielding

$$\left(2\rho T^{-1} - \frac{\Delta t}{2}R - \frac{\Delta t^2}{2}L\right)\mathbf{w}^{n+1} = -\left(2\rho T^{-1} + \frac{\Delta t}{2}R - \frac{\Delta t^2}{2}L\right)\mathbf{w}^{n-1} + 4\rho T^{-1}\mathbf{w}^n + \Delta t^2(\rho\,\mathbf{q}_t^{n+1} + \rho\,\mathbf{q}_t^{n-1}). \tag{4.2}$$

All operators present are time independent. Thus, the LU decomposition of the operator attached to $\mathbf{w}^{n+1}$ can be pre-computed and the computational cost of each time step is quadratic in the number of grid variables. Further, as will be demonstrated, this scheme is unconditionally stable leading to significantly improved computation times. For simplicity, we supply initial conditions of the form $w(x, y, 0)$ and $w(x, y, \Delta t)$. In light of (2.12), it would be sufficient to supply $P(x, y, 0)$ in place of $w(x, y, \Delta t)$.

There are two primary computational difficulties associated with any computational procedure dealing with Eq. (3.12). First, one has to be able to compute the non-constant biharmonic operator $\triangle(k(x)\triangle w)$ efficiently. Consider the expanded form of

$$\triangle(k(x)\triangle w) = \triangle k\triangle w + 2(k_x\triangle w_x + k_y\triangle w_y) + k\triangle^2 w, \tag{4.3}$$

where for our purposes $k_y = 0$. For the constant stiffness biharmonic operator, we use a second-order compact scheme due to Stephenson [18]

$$\begin{aligned}(\triangle^2 w)_{i,j} = \frac{1}{h^4}\Bigg(&56w_{i,j} - 16(w_{i+1,j} + w_{i-1,j} + w_{i,j+1} + w_{i,j-1})\\ &+ 2(w_{i+1,j+1} + w_{i+1,j-1} + w_{i-1,j+1} + w_{i-1,j-1})\\ &+ 3h\left(\frac{\partial w}{\partial x}_{i+1,j} - \frac{\partial w}{\partial x}_{i-1,j} + \frac{\partial w}{\partial y}_{i,j+1} - \frac{\partial w}{\partial y}_{i,j-1}\right)\Bigg),\end{aligned} \tag{4.4}$$

where $h = \Delta x = \Delta y$. This discretization requires values of not only w, but also of w_x and w_y. These values are computed via

$$\begin{aligned}\frac{\partial w}{\partial x}_{i,j} &= \frac{3}{4h}(w_{i+1,j} - w_{i-1,j}) - \frac{1}{4}\left(\frac{\partial w}{\partial x}_{i+1,j} + \frac{\partial w}{\partial x}_{i-1,j}\right),\\ \frac{\partial w}{\partial y}_{i,j} &= \frac{3}{4h}(w_{i,j+1} - w_{i,j-1}) - \frac{1}{4}\left(\frac{\partial w}{\partial y}_{i,j+1} + \frac{\partial w}{\partial y}_{i,j-1}\right).\end{aligned} \tag{4.5}$$

The remaining terms in (4.3) are dealt with using standard centered difference approximations for the Laplace operator. This is reasonable as values of w_x, w_y are already being utilized by the Stephenson scheme. The primary downside to this discretization is that it requires $\Delta x = \Delta y$. This will become a significant restriction in the presence of small geometric aspect ratios. We use this descriptive definition of the biharmonic discretization to produce the matrix L.

The second computational difficulty associated with this model is the DtN operator $\bar{T}$. An interesting feature of this operator is that it can be computed efficiently with the use of an FFT through the decomposition

$$\bar{T} = \mathcal{F}^{-1} D \mathcal{F}, \tag{4.6}$$

where $\mathcal{F}$ is a sin–cos Fourier transform, and D is a diagonal weighting operator. While this description provides an efficient manner of computing $\bar{T}$ in an explicit scheme, it is not used in the current implicit scheme as the matrix T is lumped with other operators before computations occur. As stated earlier, the downside of this operator is that it is linearly unbounded. This cannot, under any reasonable circumstances, be avoided as the normal derivative in Eq. (2.10) must be represented in some form. To compute with this operator we truncate it so that only N and M Fourier modes are considered in the x and y directions respectively. The resulting truncated operator has norm

$$\|\bar{T}\| \propto s_{N,M} \pi \tanh(s_{N,M} \pi L_z), \tag{4.7}$$

where $s_{N,M}$ were defined as in Eq. (3.8).

This scheme is unconditionally stable and runs in reasonable amounts of time on a standard PC. A few bottlenecks still exist in this scheme however. From a mathematical standpoint, the matrix L is sparse and T can be dealt with efficiently with an FFT. However, the given scheme requires the inversion of a matrix which lumps these together, thus negating these properties. From a practical standpoint, when computing at aspect ratios of roughly 0.015, storage of the given matrix operators becomes an issue on the standard PC system and clusters on which we work. Due to this limitation, at physiological aspect ratios, we have been limited to computations with $N + 1 = 7$ points in the lateral (y) direction. However, even at these grid sizes, computation times are still not a substantial issue and the performance of this implicit scheme is far superior to that of the aforementioned explicit scheme.

5. Convergence Results

For test purposes, we consider a modified form of the problem (3.12) given by

$$2\rho w_{tt} - \bar{T}(r(x) w_t + \triangle(k(x) \triangle w) + B_1(x, y, t)) = B_2(x, y, t) \tag{5.1}$$

and take $\rho = 1$. We use the method of manufactured solutions to test the code. A known test function w is chosen, B_1 is then selected so that the compound term $r(x)w_t + \triangle(k(x)\triangle w) + B_1$ has the appropriate spectral representation, and finally B_2 is chosen to balance the equation. The choice of B_1 serves a twofold purpose here. Recall that $\bar{T}$ must act on functions which are expandable in a particular Fourier basis. In simulations, we guarantee this by imposing the necessary boundary conditions inherited from the potential problem. However, when non-constant mechanical coefficients $r(x)$ and $k(x)$ along with w are chosen for the test problem, the resulting compound term will not in general be naturally representable in the

spectral basis associated with $\bar{T}$. We use the inhomogeneity B_1 to guarantee that in (5.1), the compound term on which $\bar{T}$ acts can be naturally represented in the basis $\{\sin\frac{n\pi x}{L_x}\cos\frac{m\pi y}{L_y}\}$. Moreover, we choose B_1 in such a way that this compound term is known in an exact form so that after $\bar{T}$ is applied, B_2 can be analytically determined.

Tests of the numerical scheme (4.2) are performed in the context presented in Sec. 6. That is, we take

$$k(x) = \epsilon k_0 \exp\left(-\lambda\frac{x}{L_x}\right), \quad r(x) = \frac{1}{\epsilon^2} \tag{5.2}$$

in order to match the scalings present in the asymptotics. The exponential decay of stiffness is chosen to match the profile seen in experimental data. We use a decay coefficient of $\lambda = 4$ per unit length yielding two orders of magnitude of decay. There seems to still be debate over the precise value of this constant. However, its particular value serves primarily as a tuning constant. As we are primarily interested in qualitative results, we do not seek to precisely match this parameter. Friction is taken to be constant over the length of the plate for lack of any specific knowledge on its form. Data not presented suggests that any nonincreasing r will lead to the same salient features to be presented with only tuning differences.

Numerous tests of this numerical scheme were performed with similar results. One representative set of tests is presented at an aspect ratio of $\epsilon = 1/32$ with input test function

$$w(x,y,t) = \sin t \sin(3\pi x)\cos\left(\frac{3\pi y}{\epsilon}\right). \tag{5.3}$$

All tests presented were performed as discussed above with exact initial data supplied at $t = 0, \Delta t$. The code was run until it was clear that transients due to initial data were damped out and L^∞ errors were recorded. Results of these tests are shown in Table 1. Similar tests were performed with different initial data. As expected, this did not affect the long term errors. Additionally, L^1 and L^2 errors exhibit the same characteristics as the L^∞ errors.

Table 1. Errors for the numerical scheme (4.2). For this test, mechanical coefficients are prescribed as (5.2). The exact solution is taken to be $w(x,y,t) = \sin t \sin(3\pi x)\cos(3\pi y/\epsilon)$. All errors are L^∞ errors measured at $t = 10\epsilon$.

Δt	$N = 6$	$N = 12$
$\frac{1}{10}$	$2.63E(-1)$	$2.97E(-1)$
$\frac{1}{50}$	$5.25E(-2)$	$6.03E(-2)$
$\frac{1}{100}$	$2.68E(-2)$	$3.02E(-2)$
$\frac{1}{200}$	$1.34E(-2)$	$1.51E(-2)$
$\frac{1}{400}$	$6.68E(-3)$	$7.54E(-3)$

This data shows the scheme is indeed $O(\Delta t)$ and unconditionally stable as expected. Further, plots of error versus time show that errors oscillate in phase with velocity w_t. This data additionally shows an increase in errors when moving from $N = 6$ to $N = 12$ lateral intervals. Additional tests not presented show that while grid refinement does sometimes increase errors, the errors converge to a time step dependent constant which exhibits the discussed linear order of convergence. It is of course necessary to use more grid points when the spatial profile becomes more complex. We will use a value of $N = 12$ for all future simulations at $\epsilon = \frac{1}{32}$. This is sufficient to capture a relatively simple lateral displacement profile. Further, this yields 385 grid points in the longitudinal direction which should be sufficient for passive simulations.

6. An Asymptotic Reduction

Due to the mathematical and computational complexities associated with three-dimensional cochlear models, much work has been done on producing and understanding reduced models. Some discussion of them can be seen in [9]. We will concentrate on the treatment of plate stiffness in such models. The most widely studied class of reduced models are those of the transmission line type [14, 13]. Such models effectively assume that the basilar membrane is a collection of uncoupled point oscillators coupled through one-dimensional fluid movements. These models can be arrived at through asymptotic reductions of three-dimensional models as in [13]. This particular reduction, due to Peskin, includes plate stiffness (with clamped boundary conditions) in a static fashion only however. Asymptotics are performed on a static plate problem and dynamics are later added.

Similar issues are present with two-dimensional models. The plate treatment in some, such as [12] due to Neely, is similar to that of a transmission line model with a two-dimensional fluid attached. Allen and Sondhi [1] maintain longitudinal (x-direction) stiffness in their treatment but remove lateral stiffness (y-direction) by assuming the y dependence of w is a centered half cosine. This is backward in some sense as the lateral direction is more energetic than the longitudinal one due to the small aspect ratio present. Similar use of a simplified lateral dependence of w is utilized even in the three-dimensional WKB model due to Steele and Lim [10]. This is by no means a comprehensive list, but it is representative of the manner in which stiffness, particularly lateral stiffness, is treated in reduced models. Such treatments, while successful, overlook valuable information relating to the stiffness and aspect ratio. We present an asymptotic reduction which does not utilize such methods.

Consider the cochlear model given by (2.11) with boundary conditions (2.12), (2.8)–(2.10) and let $L_x = 1$, $L_y = L_z = \epsilon$, where $\epsilon \ll 1$. This is a reasonable assumption given the dimensions of the human cochlea which are roughly $35 \times 0.3 \times 2\,\text{mm}$. Again assume that the input forcing is piston-like so that $F(y, z, t) = F(t)$. Now make the canonical independent variable scalings

$$y^* = \frac{y}{\epsilon}, \quad z^* = \frac{z}{\epsilon}, \quad t^* = \frac{t}{\epsilon} \tag{6.1}$$

along with

$$w = \epsilon^2 w^*. \tag{6.2}$$

The purpose of the spatial scalings is clear. The temporal scaling is made out of necessity and will be discussed in further detail later, and the scaling of the deflection w is a statement that the plate deflection must be much smaller than the depth of the cochlea. Let us now assume that ϕ takes the form

$$\phi = \phi^0 + \epsilon^2 \phi^1. \tag{6.3}$$

Upon making these substitutions in (2.11), dropping the $*$ and considering the $O(1)$ terms, it is found that

$$\phi^0 = \phi^0(x,t), \quad \phi^0(0,t) = F(t), \quad \phi^0(1,t) = 0. \tag{6.4}$$

Further considering the $O(\epsilon^2)$ terms yields the relation

$$\phi^0_{xx} = -(\phi^1_{yy} + \phi^1_{zz}), \quad \phi^1_z(x,y,0,t) = w_t \tag{6.5}$$

with homogeneous Neumann conditions for ϕ^1 on the $y = 0, 1$ and $z = 1$ faces. Integrating this with respect to y and z and applying the divergence theorem yields

$$\phi^0_{xx}(x,t) = \int_0^1 w_t(x,y,t)\, dy. \tag{6.6}$$

Now consider the elasticity equation (2.12). Upon making the above-mentioned substitutions and dropping the $*$, the meaningful (in a dominant balance sense) terms that persist are

$$r(x)\epsilon w_t + \frac{1}{\epsilon^2} k(x) w_{yyyy} = \frac{1}{\epsilon} 2\phi^0_t. \tag{6.7}$$

We now make the following scalings for k and r

$$k = \epsilon k^*, \quad r = \frac{r^*}{\epsilon^2}. \tag{6.8}$$

Here the stiffness scaling is made with energetic concerns in mind. Consider a thin clamped rod. In order to produce meaningful deflections in such a rod, it is necessary to have a large forcing, a small stiffness, or both. As this system is set up, both are present. Consider the forcing to this system $F(t)$. The relation (2.1) along with the given time scale shows that the forcing to the system is of size $O(1/\epsilon)$. The friction scaling was originally made in order for dominant balances to work out. However, there is a physical grounding behind this scaling as well. Due to the use of an inertial fluid, the only source of energy dissipation is the plate friction. Due to the large forcing present, a large friction coefficient must also be present in order for the power-in to match the power-out at the given deflection levels. Upon making these substitutions and again dropping the $*$, the dominant balance becomes

$$r(x) w_t(x,y,t) + k(x) w_{yyyy}(x,y,t) = 2\phi^0_t(x,t). \tag{6.9}$$

A complete asymptotic model is now defined by (6.4), (6.6), (6.9) with clamped boundary conditions at the $y = 0, 1$ edges for the w. Notice that unlike quantum graph models [16] where the lateral coordinate is integrated out of the reduced model, the boundary conditions in the present case imply that we must maintain the y coordinate. However, in the reduced model we are able to separate the x and y coordinates, and thus the model is structurally simpler than the original equations.

Due to the removal of clamped conditions for the plate at $x = 0, 1$ in this reduction, an associated boundary layer for w will be present. The size of such boundary layers can be analytically determined to be $O(\epsilon)$. This is also observed in Fig. 4 showing simulation results of the full cochlear problem over a range of aspect ratios. These boundary layers do not substantially effect the model and their discussion is left for future work.

This reduced model is similar in structure to a transmission line type model with the exception that the lateral direction and its associated elasticity are maintained. The dimensional reduction of ϕ seen in the transmission line type models is seen here as well and the shallow water approximation explicitly performed in previous reductions shows up in the form of the ϕ^0_{xx} term. A strength of this reduction is that it does not impose an artificial functional form on the displacement w. This does unfortunately come at the expense of an increased model complexity. Further, these asymptotics naturally separate the longitudinal complexities imposed by the fluid and variation of mechanical coefficients from the lateral complexity associated with the primary plate stiffness. In later sections we provide validation of these asymptotics and discuss a physiological result which is found during this reduction and is testable against experimental data.

7. Simulations of the Cochlea

We now present simulations of the full cochlear model (3.12) with a twofold purpose. First, we will show that this model does exhibit a crude place principle where higher input frequencies push deflections closer to the $x = 0$ end. Second, we will use simulations of the full model to validate the asymptotic reduction previously discussed. All simulations will be run in the setting discussed in the above asymptotics. Since the cochlea has a small aspect ratio, we assume the spatial dimensions are scaled so that $L_x = 1$ and set $L_y = L_z = \epsilon$, as discussed previously. We choose the plate's mechanical coefficients as shown in (5.2) with $\lambda = 4$. Finally, we express the forcing at the oval window in the form

$$F'(t) = \frac{1}{\epsilon} \sin\left(\frac{2\pi\Omega t}{\epsilon}\right) \tag{7.1}$$

to match the setting discussed previously where it is assumed that time is scaled to seconds.

A successful model of the cochlea must at the very least exhibit a place principle. That is, it must exhibit the dispersive relation where low input frequencies produce maximum response near the apical ($x = 1$) end of the partition and high frequencies

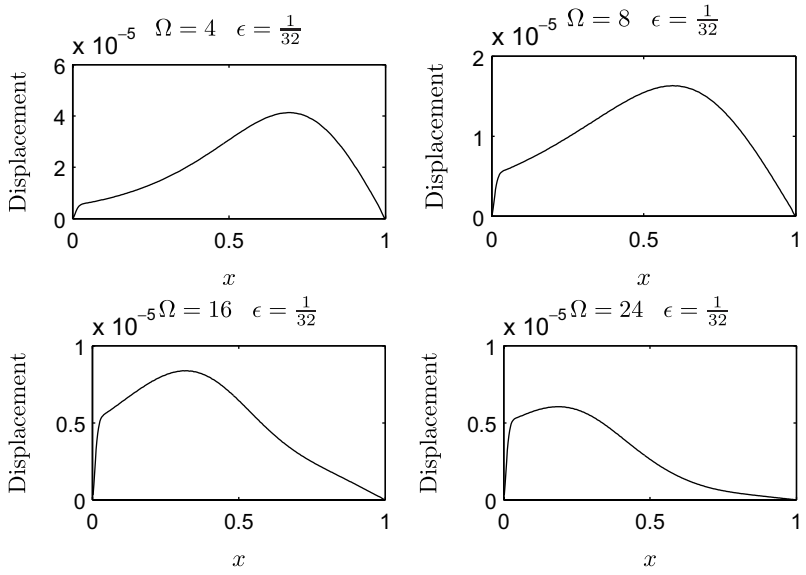

Fig. 2. These figures represent maximal deflection of the centerline of the cochlear plate as a function of location over a range of input frequencies. Computations are performed on the domain $[0,1] \times [0,\epsilon]$ with $r = 1$, $\rho = 1/2$, $\lambda = 4$, and $k_0 = 1$.

produce maximum response near the basal ($x = 0$) end of the partition. The first set of simulations depicted in Fig. 2 shows this model does indeed exhibit a crude place principle. These simulations at $\epsilon = 1/32$ show the effect of varying the scaled input frequency Ω. Based on the data in Table 1, the time step is taken to be four percent of the characteristic time scale ϵ/Ω. All simulations are run for 10 time units. After initial transients are dissipated, maximal deflections as a function of position are determined. As expected, deflection profiles are symmetric about the center-line $y = \epsilon/2$. Plots of maximal deflection of the center-line as a function of the longitudinal position x are presented in Fig. 2.

There is an additional fact not shown in the presented data. Although not apparent in the given figures, animations associated with these simulations show a clear traveling wave character with envelopes shown in Fig. 2. But for lower values of $\Omega = 1, 2$, the entire membrane vibrates as a single entity. While this is not in line with the place theory, it is in agreement with a phase locking theory. Such a theory asserts that at low input frequencies (in the range of the firing rate of the auditory nerve and below), the entire basilar membrane vibrates as a single entity and the neural firing rate encodes the signal. It is only at higher input frequencies that the place principle becomes the primary transduction mechanism. Simulation results are in line with this melding of theories.

A second set of simulations, depicted in Fig. 4 considers the effect of varying ϵ. All simulations are run in similar fashion to those already discussed. A value of $N = 12$ is used for all simulations except $\epsilon = 1/64$, where $N = 6$ is used due to

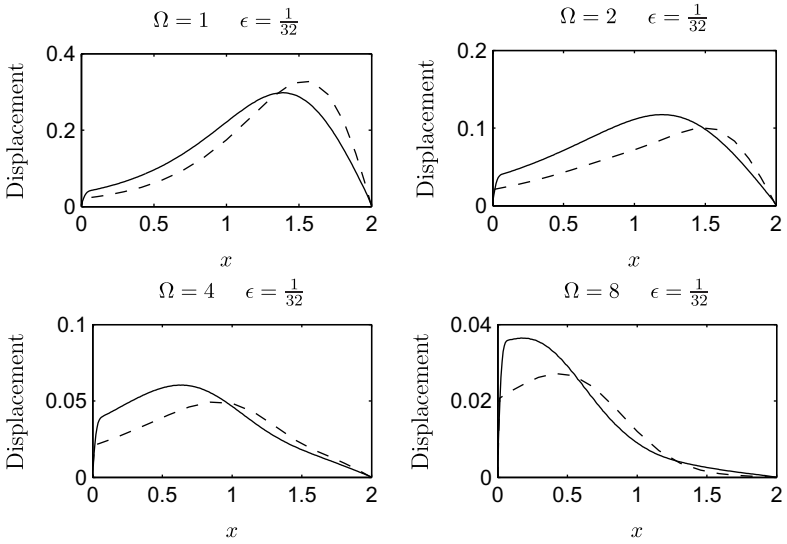

Fig. 3. These figures represent maximal deflection as a function of x for the full and reduced cochlear problems. Dashed lines represent asymptotic model simulations and full lines represent full model simulations. Full model simulations are scaled by w/ϵ^2 as in the performed asymptotics. Full model simulations are run on the domain $[0, 2] \times [0, 2\epsilon]$ and reduced model simulations on the domain $[0, 2] \times [0, 2]$ for computational reasons associated with the reduced model not discussed here. Friction and stiffness are chosen so that the full model simulations scale to the reduced model simulations with respect to ϵ. In the reduced model, we take $\rho = 1$, $r = 1$, $k_0 = 4$, and $\lambda = 4$.

memory constraints. This data suggests the asymptotics discussed in Sec. 6 hold at least at a cursory level. The four presented plots show nearly identical profiles. They do differ in scale as expected due to the $w = \epsilon^2 w^*$ scaling followed closely by this data. Further differences are seen near $x = 0$. This is the result of a boundary layer caused by the clamped condition discussed briefly in Sec. 6.

In addition, we make a direct comparison between simulations of the full and reduced models in Fig. 3. These plots overlay deflection envelopes found in full model (scaled by ϵ^2) and reduced model simulations. Reduced model simulations are performed using a Chebyshev collocation method [3] not discussed here. For computational simplicity associated with this method, we work on the domain $[0, 2] \times [0, 2]$ and scale the domain in full model simulations accordingly. Deflection levels and shapes over the range of frequencies show good agreement given the complexity of the problem being discussed. This provides more direct validation of these asymptotics.

8. A Discussion of ϵ as a Time/Frequency Scale

We now return to an issue which has been avoided to this point. Recall that in the asymptotic derivation, the time scaling $t^* = t/\epsilon$ was necessary. This scaling is now used to provide more qualitative support for the asymptotics performed as well as

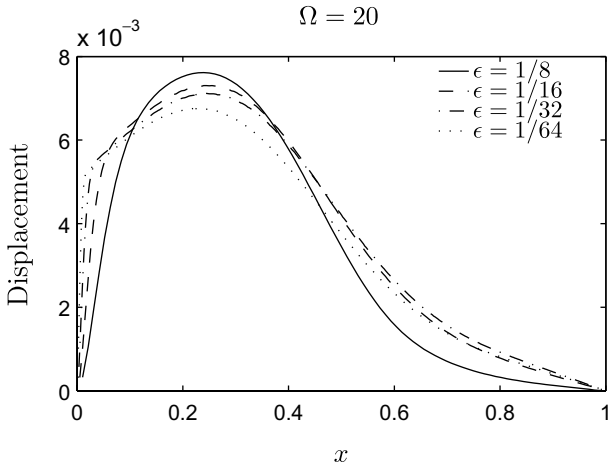

Fig. 4. These figures represent maximal deflection of the centerline of the cochlear plate as a function of location for a fixed input frequency $\Omega = 20$ over a range of aspect ratios. In all cases w is scaled by ϵ^2 as in the presented asymptotics for comparison purposes. Computations are performed with $r = 1$, $\rho = 1/2$, $\lambda = 4$, and $k_0 = 1$.

an interesting result relating the form and function of the cochlea. Consider Fig. 4. Here, the full model is simulated with all input scalings accounted for as in the reduced model with only ϵ varying. It is clear that the structure of these solutions is independent of this parameter, thus lending support for the proposed asymptotic reduction.

There is more to be said about the proposed time scaling. View this instead as a frequency scaling; the effective input frequencies for the simulations shown in Fig. 4 are Ω/ϵ as opposed to simply Ω. While the four deflection plots presented all have the same value for Ω, their true frequencies take the values $160, 320, 640, 1280$ Hz. Thus, as the aspect ratio ϵ is decreased, the size of the input frequency necessary to produce a specific deflection map (or to excite a particular characteristic place) increases. This suggests the size of the effective hearing band, denoted $|HB|$, is inversely related to the aspect ratio

$$|HB| \propto \frac{1}{\epsilon}. \tag{8.1}$$

In order to test this we have found data relating to five mammals with comparably sized hearing bands. Table 2 shows that for these five mammals, the cochlear aspect ratios are in the same range. It is difficult to make a strong statement about the validity of (8.1) based on this data alone as there is a good deal of spread. However, the fact that all five species have aspect ratios in the same range lends some credence to this statement. When considering this data, keep in mind that the stated aspect ratios relate to the width of the basilar membrane at the apex only. Given the tapered nature of the basilar membrane, it is likely that a result of this form would require some form of an effective aspect ratio for tight comparison.

Table 2. This table represents hearing band and aspect ratio data for five mammal species. Aspect ratio data was taken directly from [11].

	$\|HB\|$ (Octaves)	BM length (mm)	BM apex width (μm)	ϵ
Gerbil	10	12.1	250	0.0207
Chinchilla	9	18.5	310	0.0168
Cat	10	25.8	420	0.0163
Guine Pig	10	18.5	245	0.0132
Human	9+	33.5	504	0.0150

9. Concluding Remarks

We presented a numerical solution of the three-dimensional hydro-elastic equations of a model cochlea. Due to the small aspect ratio and the clamped nature of the basilar membrane, its deflection is small. We therefore used a linear fluid model and linear coupling between the fluid and the plate. Although our fluid model is inviscid and irrotational, our formulation is quite general. One can replace the fluid model by another model simply by changing the DtN operator used here to another DtN operator that fits a different fluid model.

A key idea in our work is that we model the basilar membrane as a nonhomogeneous plate in which stiffness is decaying as one proceeds from the basal end to the apical end of it. This variable elastic coefficient is responsible for the dispersion effects observed in the cochlea, and thus the place principle whereby inputs with higher frequencies give rise to maximal deflections closer to the basal end. Indeed our numerics exhibit such a place principle.

It is well known that the passive mechanics of the cochlea cannot fully account for its observed behavior [2, 15]. It is believed that the complex microstructure (Organ of Corti) sitting atop the basilar membrane provides an active feedback on its motion [15]. There is still much debate over the form and function of this feedback, but there is compelling evidence that cochlear hair cells are responsible. The Organ of Corti has four rows of hair cells running the length of the cochlea consisting of one row of inner hair cells (IHC) and three rows of outer hair cells (OHC). The IHC's are passive and serve primarily as a neural transducer. The OHC's are known to be motile. It is believed that this motility acts as a mechanical amplifier by feeding energy into the passive traveling wave [15]. The specific manner in which this occurs is not well understood. While the place principle seen in our numerical model is not highly localized, we believe that including an active ingredient in the model, a more localized response will ensue.

In addition, we provide an asymptotic reduction of the model equations with energetic concerns in mind. We provided evidence (both indirect and direct) that these asymptotics are valid. In the process of performing this asymptotic analysis, it was found that a time scale related to the cochlear aspect ratio appeared in the problem. The presence of this time/frequency scale is verified with full model simulations. We further proposed a physiological result relating the form and function

of the cochlea which was compared to physiological data. While this comparison lent credence to the stated result, further verification is necessary.

References

1. J. B. Allen and M. M. Sondhi, Cochlear macromechanics: Time domain solutions, *J. Acoust. Soc. Am.* **66** (1979) 123–132.
2. G. V. Bekesy, *Experiments in Hearing* (McGraw-Hill, 1960).
3. J. P. Boyd, *Chebyshev and Fourier Spectral Methods*, 2nd edn. (Dover, 2001).
4. E. Givelberg and J. Bunn, A comprehensive three-dimensional model of the cochlea, *J. Comput. Phys.* **191** (2003) 377–391.
5. J. Keener and J. Sneyd, *Mathematical Physiology* (Springer, 2001).
6. J. B. Keller and J. C. Neu, Asymptotic analysis of a viscous cochlear model, *J. Acoust. Soc. Am.* **77** (1985) 2107–2110.
7. Y. Kim and J. Xin, A two-dimensional nonlinear nonlocal feed-forward cochlear mode and time domain computation of multitone interactions, *Multiscale Model. Simul.* **4** (2005) 664–690.
8. L. Landau and E. Lifshitz, *Theory of Elasticity*, Course of Theoretical Physics, Vol. 7, 3rd edn. (Elsevier, 1986).
9. J. Lighthill, Energy flow in the cochlea, *J. Fluid Mech.* **106** (1981) 149–213.
10. K.-M. Lim and C. R. Steele, A three-dimensional nonlinear active cochlear model analyzed by the WKB-numeric method, *Hearing Res.* **170** (2002) 190–205.
11. D. Manoussaki, R. S. Chadwick, D. R. Ketten, J. Arruda, E. K. Dimitriadis and J. T. O'Malley, The influence of cochlear shape on low-frequency hearing, *PNAS* **105** (2008) 6162–6166.
12. S. T. Neely, Finite difference solution of a two-dimensional mathematical model of the cochlea, *J. Acoust. Soc. Am.* **69** (1981) 1386–1393.
13. C. S. Peskin, *Partial Differential Equations in Biology.* Courant Inst. Lecture Notes. (Courant Institute of Mathematical Sciences, 1975–76).
14. L. C. Peterson and B. P. Bogert, A dynamical theory of the cochlea, *J. Acoust. Soc. Am.* **22** (1950) 369–381.
15. J. O. Pickles, *An Introduction to the Physiology of Hearing*, 3rd edn. (Emerald, 2008).
16. J. Rubinstein and M. Schatzman, Variational problems in multiply connected thin strips I: Basic estimates and convergence of the Laplacian spectrum, *Arch. Rational Mech. Anal.* **160** (2001) 271–308.
17. C. R. Steele, Behavior of the basilar membrane with pure-tone excitation, *J. Acoust. Soc. Am.* **55** (1974) 148–162.
18. J. W. Stephenson, Single cell discretizations of order two and four for biharmonic problems, *J. Comput. Phys.* **55** (1984) 65–80.
19. J. Xin, Y. Qi and L. Deng, Time domain computation of a nonlinear nonlocal cochlear model with applications to multitone interaction in hearing, *Comm. Math. Sci.* **1** (2003) 211–227.